pressures of about 1 MPa reaching the focal zone (Fig. 3B).

The frequency and magnitude of seismic events reached a climax between May 2012 and September 2013, when more than 80% of events occurred, including four $M_w \geq 4$ earthquakes. This period of elevated seismic activity followed a rapid decline in injection at the west wells (Fig. 3B). Thus, the timing of seismicity may be determined by pore pressure diffusion to the depths of the earthquakes. Additional contributions to the stresses may also promote seismicity, such as from the poroelastic stresses near the well that accompany the decrease in injection. For an optimally oriented strike-slip fault with the fault-normal direction radial to the injection site, a sudden decline in injection rate relaxes the compressive stress (*34*). All of the seismic events discussed here occurred on a fault with the fault-normal direction oriented at N60°E, radial to the west injection wells.

Our coupled flow and poroelastic model allows us to predict the future pore pressure distribution after injection ends (Fig. 3A). As injection ends in the west wells by about 2016, the model shows the pressure decreasing approximately exponentially. However, the decay rate is fastest in the most permeable formations and at the depths where injection occurs. At the east wells, 10 years after shut-off, the pore pressure remains close to its maximum level. For the west wells, only 5 years after a hypothesized shut-off, pore pressure drops to less than 10% of its maximum value. This observation has direct implications for future injection operations and seismic hazard estimations. Changes in the seismicity rate are a function of changes in Coulomb stress and background stress (*35*). Our study shows that the background stress is characterized by a relaxation time that depends on both the injection history and hydrogeological properties. Therefore, injection history at a given site may modify future estimates of the seismic hazard.

Better quantification of the evolution of the stress and pore pressure in the crust is vital to forecasting fault reactivation (*9*, *36*). Despite improvements in seismic monitoring capacity and the resulting decrease in the magnitude detection threshold (*37*, *38*), observations of the in situ pore pressure and stress field remain elusive because of the scarcity of deformation observations and limited integration of those observations with physical models. This work highlights the value of monitoring surface deformation, in particular by using advanced remote sensing techniques, to understand the evolution of pore pressure and stress at depth. The ability to measure crustal stress evolution affords a proactive approach to managing the hazard associated with fluid injection. Observation of the time-dependent stress field permits the construction of temporally variable statistical frameworks (*34*), which are useful for earthquake operational forecasting (*39*). The key to successful operational earthquake hazard assessment is being able to continuously update information about the probability of a future earthquake, which can be achieved by using data and models such as those presented in this study. Geodetic monitoring and modeling schemes are valuable components of efforts to mitigate induced seismic hazard.

REFERENCES AND NOTES

1. J. L. Rubinstein, A. B. Mahani, *Seismol. Res. Lett.* **86**, 1060–1067 (2015).
2. M. Weingarten, S. Ge, J. W. Godt, B. A. Bekins, J. L. Rubinstein, *Science* **348**, 1336–1340 (2015).
3. M. J. Hornbach *et al.*, *Nat. Commun.* **6**, 6728 (2015).
4. K. M. Keranen, H. M. Savage, G. A. Abers, E. S. Cochran, *Geology* **41**, 699–702 (2013).
5. C. Frohlich *et al.*, *J. Geophys. Res. Solid Earth* **119**, 581–593 (2014).
6. C. Frohlich, E. Potter, C. Hayward, B. Stump, *Leading Edge* **29**, 270–275 (2010).
7. S. Horton, *Seismol. Res. Lett.* **83**, 250–260 (2012).
8. F. R. Walsh 3rd, M. D. Zoback, *Sci. Adv.* **1**, e1500195 (2015).
9. W. L. Ellsworth, *Science* **341**, 1225942 (2013).
10. W. H. Granata, *Cretaceous Stratigraphy and Structural Development of the Sabine Uplift Area, Texas and Louisiana* (Shreveport Geological Society, 1963).
11. Z. Fan, P. Eichhubl, J. F. Gale, *J. Geophys. Res. Solid Earth* **121**, 2798–2812 (2016).
12. P. A. Hsieh, J. D. Bredehoeft, *J. Geophys. Res.* **86**, 903–920 (1981).
13. K. M. Keranen, M. Weingarten, G. A. Abers, B. A. Bekins, S. Ge, *Science* **345**, 448–451 (2014).
14. C. B. Raleigh, J. H. Healy, J. D. Bredehoeft, *Science* **191**, 1230 (1976).
15. Y. Zhang *et al.*, *Ground Water* **51**, 525–538 (2013).
16. Y. Guglielmi, F. Cappa, J.-P. Avouac, P. Henry, D. Elsworth, *Science* **348**, 1224–1226 (2015).
17. P. Segall, *J. Geophys. Res. Solid Earth* **90**, 6801 (1985).
18. J. Du, J. E. Olson, *J. Petrol. Sci. Eng.* **30**, 181–197 (2001).
19. Z. R. Chen, *J. Petrol. Sci. Eng.* **80**, 41–52 (2011).
20. D. W. Vasco *et al.*, *Geophys. Res. Lett.* **37**, L03303 (2010).
21. M. Shirzaei, *IEEE Geosci. Remote Sens. Lett.* **10**, 456–460 (2013).
22. Materials and methods are available as supplementary materials on *Science* Online.
23. A. Mossop, P. Segall, *J. Geophys. Res. Solid Earth* **104**, 29113–29131 (1999).
24. E. A. Roeloffs, in *Advances in Geophysics*, R. Dmowska, Ed. (Academic Press, 1996).
25. A. Y. Rozhko, Y. Y. Podladchikov, F. Renard, *Geophys. Res. Lett.* **34**, L22304 (2007).
26. S. Rojstaczer, S. Wolf, *Calif. Geol.* **20**, 211 (1992).
27. Y. Kitagawa, K. Fujimori, N. Koizumi, *Geophys. Res. Lett.* **29**, 121-1–121-4 (2002).
28. E. A. Roeloffs, *Pure Appl. Geophys.* **126**, 177–209 (1988).
29. E. E. Brodsky, E. Roeloffs, D. Woodcock, I. Gall, M. Manga, *J. Geophys. Res.* **108**, 2390 (2003).
30. S. A. Shapiro, P. Audigane, J.-J. Royer, *Geophys. J. Int.* **137**, 207–213 (1999).
31. L. Seeber, J. G. Armbruster, W.-Y. Kim, *Bull. Seismol. Soc. Am.* **94**, 76–87 (2004).
32. C. Nicholson, E. Roeloffs, R. L. Wesson, *Bull. Seismol. Soc. Am.* **78**, 188 (1988).
33. C. H. Scholz, *The Mechanics of Earthquakes and Faulting* (Cambridge Univ. Press, ed. 2, 2002).
34. P. Segall, S. Lu, *J. Geophys. Res. Solid Earth* **120**, 5082–5103 (2015).
35. J. H. Dieterich, *J. Geophys. Res.* **99**, 2601–2618 (1994).
36. M. W. McClure, R. N. Horne, *GRC Trans.* **35**, 1487 (2011).
37. N. Deichmann, D. Giardini, *Seismol. Res. Lett.* **80**, 784–798 (2009).
38. W.-Y. Kim, *J. Geophys. Res. Solid Earth* **118**, 3506–3518 (2013).
39. T. H. Jordan *et al.*, *Ann. Geophys.* **54**, 315 (2011).

ACKNOWLEDGMENTS

RADARSAT-2 images were acquired under SOAR-E (Science and Operational Applications Research–Education) project 5226 of the Canadian Space Agency (www.asc-csa.gc.ca/eng/). ALOS data were obtained through Alaska Satellite Facilities (www.asf.alaska.edu/). M.S.'s contribution was supported by U.S. Geological Survey grant G13AP00040. K.F.T. was supported by a Discovery Grant from the Natural Sciences and Engineering Research Council of Canada. W.L.E. was supported by the Stanford Center for Induced and Triggered Seismicity. M.M. was supported by U.S. NSF grant EAR-1344424. P.J.G. was supported by the UK Natural Environment Research Council projects COMET and NE/K011006/1. A copy of the interferograms, LOS deformation maps, model results, and codes for InSAR processing, strain inversion, and pore pressure modeling can be obtained through the website of the Radar Remote Sensing and Tectonic Geodesy Lab (ratlab.asu.edu) or by correspondence with M.S.

SUPPLEMENTARY MATERIALS

www.sciencemag.org/content/353/6306/1416/suppl/DC1
Materials and Methods
Figs. S1 to S10
Tables S1 to S8
References (*40*–*57*)

2 May 2016; accepted 26 August 2016
10.1126/science.aag0262

CARBON CYCLE

Radiocarbon constraints imply reduced carbon uptake by soils during the 21st century

Yujie He,[1]* Susan E. Trumbore,[2] Margaret S. Torn,[3] Jennifer W. Harden,[4,5] Lydia J. S. Vaughn,[3] Steven D. Allison,[1,6] James T. Randerson[1]

Soil is the largest terrestrial carbon reservoir and may influence the sign and magnitude of carbon cycle–climate feedbacks. Many Earth system models (ESMs) estimate a significant soil carbon sink by 2100, yet the underlying carbon dynamics determining this response have not been systematically tested against observations. We used ^{14}C data from 157 globally distributed soil profiles sampled to 1-meter depth to show that ESMs underestimated the mean age of soil carbon by a factor of more than six (430 ± 50 years versus 3100 ± 1800 years). Consequently, ESMs overestimated the carbon sequestration potential of soils by a factor of nearly two (40 ± 27%). These inconsistencies suggest that ESMs must better represent carbon stabilization processes and the turnover time of slow and passive reservoirs when simulating future atmospheric carbon dioxide dynamics.

Soil carbon is a dynamic reservoir that may increase substantially in size during the 21st century, as predicted by Earth system models (ESMs), thereby influencing the sign and magnitude of carbon cycle feedbacks under climate change (*1*–*4*). Under a high radiative forcing scenario (representative concentration pathway 8.5), changes in soil carbon estimated by different models vary from a loss of 20 Pg C to a gain of more than 360 Pg C

EMBARGOED UNTIL 2PM U.S. EASTERN TIME ON THE THURSDAY BEFORE THIS DATE:

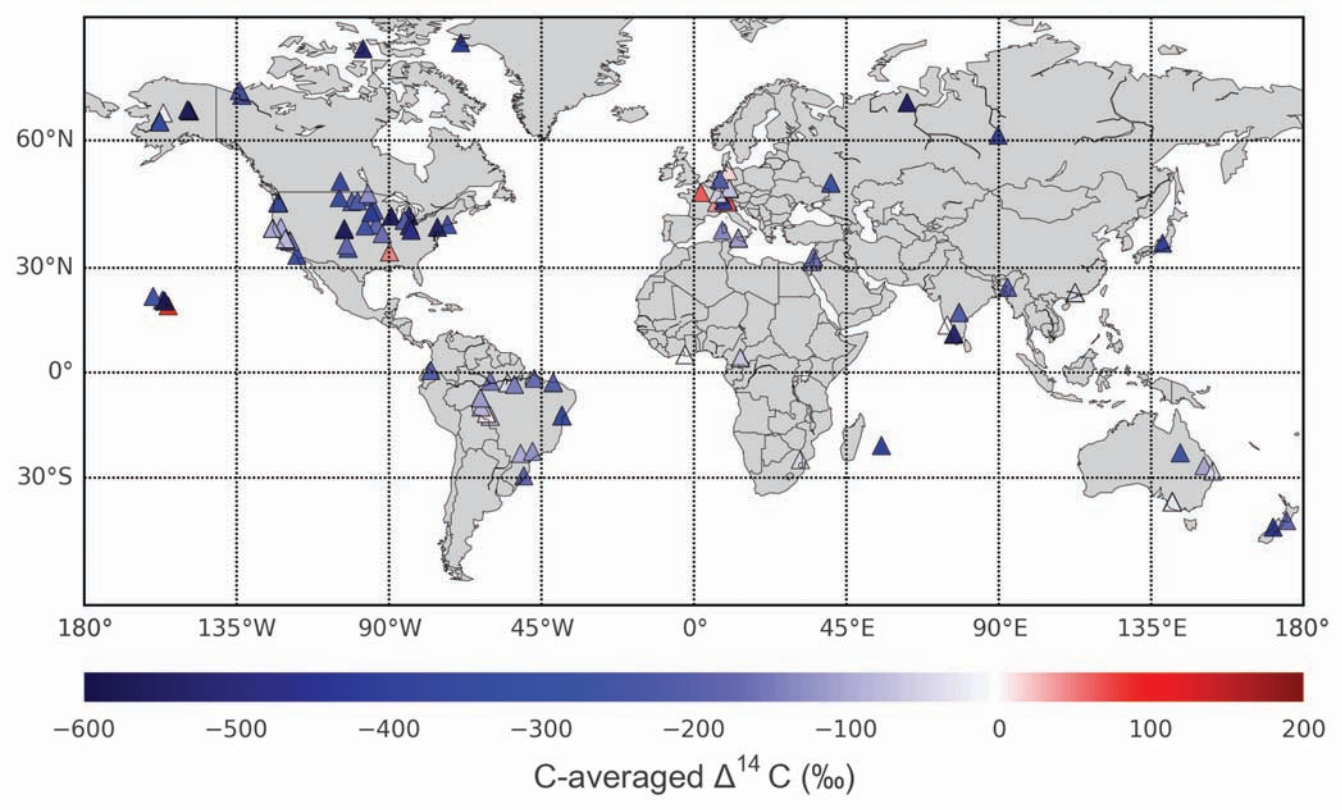

Fig. 1. Locations of radiocarbon soil profiles used to constrain ESM soil carbon mean ages and turnover times (*N* = 157). The carbon-weighted $\Delta^{14}C$ to a depth of 1 m is denoted with the color shade of each symbol. A summary of the location, sample year, and reference for each site is provided in table S2.

(*5*). These models suggest that the global carbon inventory in mineral soils may increase by 30% or more over a time span of about two centuries. The multimodel mean soil carbon accumulation of 109 Pg C (*5*) represents about one decade of global fossil fuel emissions at current rates and 5% of cumulative fossil emissions by 2100 for this scenario (*6*). This soil carbon sink represents a negative feedback on CO_2 emissions and, if robust, would slow the rate of climate change.

Still, there are substantial uncertainties in the soil carbon sink projected by ESMs (*5*). Rapid rates of carbon sequestration in ESMs contrast with findings from CO_2 and warming experiments (*7*, *8*), as well as multiple theoretical and observational constraints indicating slow (millennial) rates of soil organic carbon (SOC) accrual and turnover (*9*–*14*). Model uncertainty—as measured by intermodel spread—is high for soil carbon turnover time (τ) and exceeds the uncertainty estimated for carbon uptake through gross primary production (GPP) (*15*, *16*).

[1]Department of Earth System Science, University of California, Irvine, CA, USA. [2]Department of Biogeochemical Processes, Max-Planck-Institute for Biogeochemistry, Jena, Germany. [3]Earth Sciences Division, Lawrence Berkeley National Laboratory, Berkeley, CA, USA. [4]U.S. Geological Survey, Menlo Park, CA, USA. [5]Stanford University, Stanford, CA, USA. [6]Department of Ecology and Evolutionary Biology, University of California Irvine, Irvine, CA, USA.
***Corresponding author. Email: yujie.he@uci.edu**

In coupled model simulations, the relative sink strength (i.e., percentage change in soil carbon) depends on the responses of net primary production (NPP) and soil carbon dynamics to increasing atmospheric CO_2 concentrations and, to a lesser extent, climate change (*5*). Elevated CO_2 increases photosynthesis and NPP, which results in greater carbon inputs to soil pools with decadal or longer residence times. Carbon sequestration in soils reduces the buildup of CO_2 in the atmosphere (the carbon-concentration feedback). On the other hand, elevated CO_2 also warms the climate, which tends to accelerate soil carbon turnover and reduce carbon storage (the carbon-climate feedback) (*17*, *18*). Although these feedbacks oppose one another, the carbon-concentration feedback is more than four times as high, on average, as the carbon-climate feedback in current ESMs at the global scale (*3*). Differences in the representation of elevated CO_2 versus climate effects on ecosystem processes result in substantial variation in soil carbon sequestration estimates (*19*) (table S1).

Without a strong carbon-concentration feedback, ESMs would likely project smaller gains or larger losses of soil carbon over the 21st century. Our aim was to constrain the magnitude of the soil carbon–concentration feedback with soil radiocarbon observations. Radiocarbon content provides information about soil carbon turnover over centuries to millennia based on radioactive decay and over decades, based on inputs of ^{14}C from atmospheric weapons testing ("bomb carbon"). Accurate carbon turnover times are important for ESM projections because pools with short turnover times rapidly adjust to increasing NPP, whereas pools with long turnover times (and, by inference, low rates of inputs) change only slowly, possibly beyond the time horizon of effective climate mitigation efforts. Therefore, inaccuracies in the representation of carbon turnover times will have consequences for the rate and magnitude of the carbon-concentration feedback simulated by ESMs. Here, we used $\Delta^{14}C$ measurements at 157 sites across multiple biomes (Fig. 1 and table S2) along with carbon inventory data to constrain soil carbon dynamics in five biogeochemically coupled ESM simulations (esmFixClim1) from the Coupled Model Intercomparison Project Phase 5 (CMIP5) (*20*). In these idealized simulations, the atmospheric CO_2 mole fraction starts at a preindustrial value of 285 parts per million (ppm) and rises at a rate of 1% $year^{-1}$, thus quadrupling over 140 years. The biogeochemical components of each model experience the increasing trajectory of atmospheric CO_2, whereas the atmospheric radiation submodels do not, limiting impacts solely to the direct effects of CO_2 on plant physiology and thus enabling diagnosis of carbon-sink sensitivity to increasing CO_2.

Total initial soil carbon in the ESMs was not significantly different from the total amount in the top meter of the Harmonized World Soil Database (HWSD) (Fig. 2, A and B) for four of the five models [$P > 0.05$, except for the Community

EMBARGOED UNTIL 2PM U.S. EASTERN TIME ON THE THURSDAY BEFORE THIS DATE:

Table 1. Global soil carbon stocks and carbon uptake for CMIP5 models that experienced a quadrupling of atmospheric CO_2 from a preindustrial value of 285 ppm over a period of 140 years.

ESM	Initial SOC (Pg C)	% change in SOC	% change in SOC after ^{14}C constraint	^{14}C-imposed sink reduction (%)	τ_{slow} (year)*	$\tau_{passive}$ (year)	r_f	r_s	^{14}C-imposed correction factors† τ_{slow}	$\tau_{passive}$	r_f	r_s
CESM1 (BGC)	571	6.3	5.1	19	56 ± 16	1310 ± 241	0.06 ± 0.05	0.33 ± 0.05	–	3.7 ± 1.5	–	0.34 ± 0.75
GFDL-ESM2M	1344	26	3.3	87	231 ± 196	–	0.17 ± 0.07	–	16 ± 18	–	0.06 ± 0.14	–
HadGEM2-ES	1028	63	33	46	208 ± 84	–	0.12 ± 0.07	–	17 ± 12	–	0.07 ± 0.32	–
IPSL-CM5A-LR	1340	27	25	5.9	218 ± 82	1181 ± 347	0.06 ± 0.03	0.29 ± 0.07	–	14 ± 8.3	–	0.07 ± 0.14
MRI-ESM1‡	1403	36	22	40	347 ± 117	1065 ± 257	0.17 ± 0.09	0.10 ± 0.06	–	13 ± 7.2	0.46 ± 0.79	0.34 ± 0.74
Mean§	1137 ± 312	32 ± 18	18 ± 12	40 ± 27	212 ± 104	1185 ± 123	0.12 ± 0.06	0.24 ± 0.12	16.5 ± 0.5	10.2 ± 4.6	–	–

*τ_{slow}, $\tau_{passive}$ denote the turnover time, and r_f, r_s denote the transfer coefficient from the fast to the slow pool and from the slow to the passive pool, respectively. Reported values were estimated as an area-weighted mean and standard deviation of all model grid cells. †The mean and standard deviation of the ^{14}C-imposed correction factors were derived from using the ^{14}C observations at each site in a single optimization and then averaging these scalar adjustments across the set of 157 optimizations. ‡The ^{14}C-constrained sink reduction and correction factor for MRI were based on an inverse analysis that changed the pool size of both slow and passive pools. The reported percentage change in SOC and sink reduction were derived from transient simulations starting at steady state with the reduced complexity model. See methods in the supporting materials. §The multimodel mean and standard deviation were estimated using the mean value from each of the five ESMs.

ESM (CESM), $P = 0.03$]. Therefore, we compared ESM-derived $\Delta^{14}C$ to observations derived from soil profiles to a 1-m depth. The carbon and ^{14}C patterns of the soil profiles we used were similar to those reported in a recent synthesis paper (*21*), and we used some of the same profiles in our analysis.

Comparing ESM outputs with ^{14}C observations requires a model analysis approach because most ESMs do not yet explicitly simulate $\Delta^{14}C$ in soils, and no ESMs had reported turnover times for soil carbon pools. Therefore, we used a reduced complexity (RC) model to approximate soil carbon dynamics in each ESM. This approach allowed us to estimate the turnover times and $\Delta^{14}C$ associated with the carbon pools in different ESMs (table S3). Where possible, we used a three-pool RC model (with fast, slow, and passive pools) to simulate carbon and ^{14}C dynamics. A multipool structure is essential because radiocarbon observations show that soil carbon fluxes (NPP inputs and heterotrophic respiration) exchange mainly with short-lived pools, whereas carbon stocks are dominated by long-lived pools (*12*, *18*, *22*, *23*). The three-pool RC model had five parameters representing turnover times of fast, slow, and passive pools (τ_{fast}, τ_{slow}, and $\tau_{passive}$) and transfer coefficients

Table 2. Summary of sensitivity experiments.

Experiment	% change in SOC after ^{14}C constraint*	^{14}C-imposed sink reduction (%)*	Correction factor for turnover time*	Correction factor for transfer coefficient*
Biome-specific inversions	17 ± 11	43 ± 24	–	–
Match SOC with HWSD at sites†	18 ± 12	31 ± 40	13 ± 4.5	0.19 ± 0.23
Match SOC with 1.5*HWSD at sites†	21 ± 12	19 ± 42	11 ± 4.5	0.38 ± 0.39
–1 SD of intersite variation	14 ± 9.9	52 ± 23	–	–
+1 SD of intersite variation	23 ± 16	25 ± 25	–	–

*The mean and standard deviation were estimated from the global mean change of each of the five individual ESMs. The correction factors for the turnover time and transfer coefficients are reported for the slowest carbon pool. †The correction factors were obtained at each site, and then the mean scalar across all sites was applied to the global forward simulation.

EMBARGOED UNTIL 2PM U.S. EASTERN TIME ON THE THURSDAY BEFORE THIS DATE:

(r_f and r_s) that regulated carbon flow from the fast to slow, and slow to passive pools (fig. S1). We used a two-pool RC model for Geophysical Fluid Dynamics Laboratory model ESM2M (GFDL-ESM2M) because it represents soil carbon with two pools (*24*) and for Hadley Global Environment Model 2-ES (HadGEM2-ES) because it reported carbon for two pools (table S4). The two-pool RC model had three parameters, representing τ_{fast}, τ_{slow}, and r_f (fig. S1). After verifying that the RC model was a good approximation of each ESM based on minimization of root-mean-square error, we used the RC models to simulate $\Delta^{14}C$ values at each grid cell, with observed atmospheric $\Delta^{14}C$ for the past 50,000 years as a boundary condition and accounting for radioactive decay (see supplementary materials).

We used an inverse analysis to determine the RC model parameters that were most consistent with our $\Delta^{14}C$ data set. In the inversion, we adjusted the parameters described above to match both the total carbon and radiocarbon constraints. With these constraints, turnover time and carbon input rate for each pool were coupled such that an increase in turnover time required a compensatory decline in inputs (fig. S2). RC parameters derived from the inversion were subsequently used to assess consequences of ^{14}C constraints for the carbon-concentration feedback.

All ESMs projected an increase in soil carbon over 140 years with a multimodel mean of 32% (Table 1). This increase was primarily driven by increasing carbon inputs to soil under the quadrupling of CO_2 (table S3), as temperature increased by only a small amount (mean ± 1 SD was 0.52° ± 0.68°C) for this set of biogeochemically coupled simulations. CESM showed the smallest soil carbon increase (6.3%), primarily because of low litter inputs relative to other ESMs (table S3). For this time period and set of model runs, storage in soil carbon accounted for 42 ± 17% of the total accumulation of carbon in the terrestrial biosphere.

Both two- and three-pool RC models reproduced the global carbon dynamics of the original ESMs (fig. S3 to S5 and table S5). The τ_{fast} across all RC models was less than 20 years, whereas τ_{slow} varied from 40 to 600 years (fig. S6) with a multimodel mean of 212 ± 104 years. The mean $\tau_{passive}$ for the three-pool RC models from CESM, Institut Pierre Simon Laplace model (IPSL), and the Meteorological Research Institute model (MRI) was 1185 ± 123 years (Table 1 and fig. S7). Using the RC model parameters estimated at each grid cell within an ESM, we calculated the expected $\Delta^{14}C$. The resulting global average $\Delta^{14}C$ for 1995 (median sample year of site profiles) from the RC models was significantly higher than the mean of the observations [−6.4 ± 64 per mil (‰) versus −211 ± 156‰] (Fig. 2, C and D ($P < 0.001$). $\Delta^{14}C$ values from RC models approximating ESMs with passive pools were more negative (−53 ± 35‰) but still significantly higher than the observations ($P < 0.001$). Converting these $\Delta^{14}C$ observations into mean age for the soil profile yielded an estimate of 3100 ± 1800 years for the observed soil carbon integrated to 1 m and 430 ± 50 years for the ESMs (Fig. 2, E and F). These results indicated that the ESMs

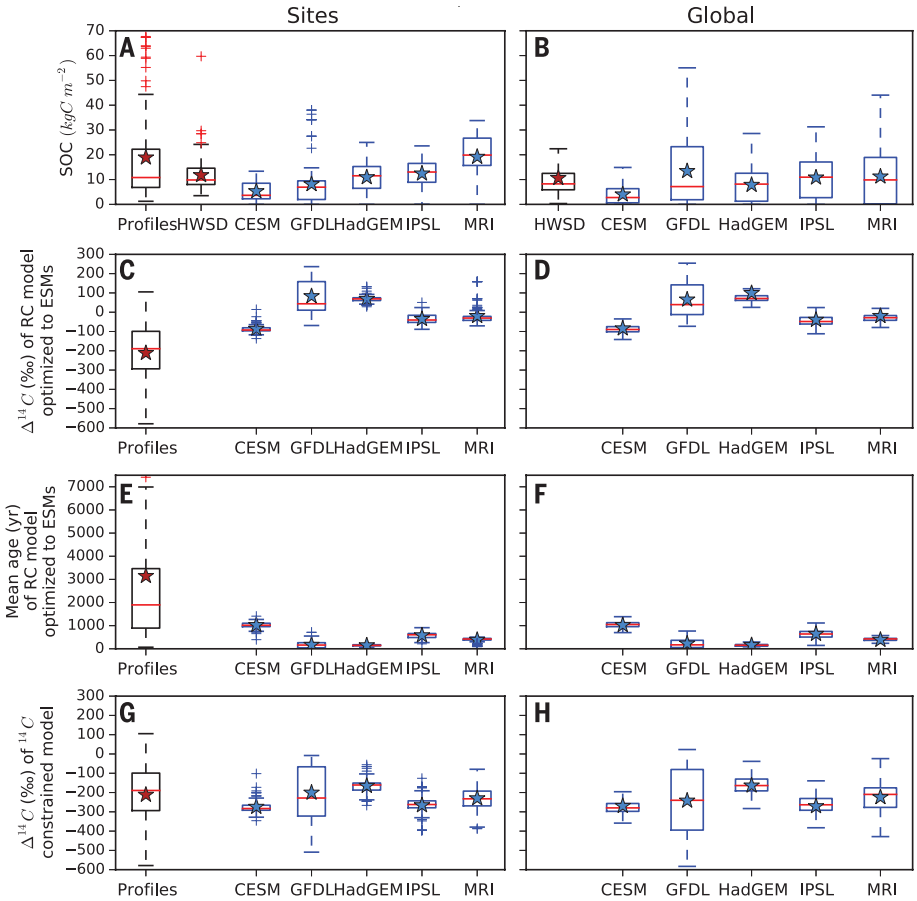

Fig. 2. Site and global values of soil carbon inventory, $\Delta^{14}C$, and mean age from observations and reduced complexity models. (**A** and **B**) SOC content of the original ESMs. (**C** and **D**) The $\Delta^{14}C$ of the reduced complexity model optimized to the original ESMs. (**E** and **F**) Corresponding mean age (**G** and **H**) The $\Delta^{14}C$ of the ^{14}C-constrained reduced complexity models. The left column shows the values of the models sampled at the locations of the individual soil profiles; the right column shows the global model distribution. Data from profile sites and the HWSD represent carbon content in the top 1 m of soil; data from ESMs are the total carbon stock. The star denotes the mean; the + symbol denotes outliers beyond the 25th and 75th percentiles.

did not have enough old carbon that had experienced substantial levels of radioactive decay; concurrently, the models assimilated too much bomb ^{14}C.

The ^{14}C-derived mean ages indicate that organic carbon soil is often thousands of years old (*12–14*, *21*), which is an order of magnitude older than suggested by ESM turnover parameters. This discrepancy is likely a consequence of incomplete representation of key biogeochemical processes and difficulties in developing accurate parameterizations for soil carbon at a global scale. Most ESMs do not account for stabilization mechanisms whereby mineral interactions and aggregate formation protect soil organic matter from decomposition over centuries to millennia (*13*, *25–28*). Moreover, first-order decay, as represented in ESMs, may not capture the response of mineral-stabilized carbon to changes in soil moisture, temperature, and other conditions (*29–31*). In addition, some ESM turnover parameters are based on laboratory incubation studies, which are often biased fast compared with in situ decomposition rates (*32*). Finally, this set of ESMs did not explicitly resolve vertical differences in soil organic matter dynamics, which may cause underestimation of turnover times in deep soils with large carbon stocks (*21*, *25*, *33*, *34*).

Because the turnover times derived from ESMs were inconsistent with ^{14}C observations, we optimized the turnover parameters by fitting our RC models to the observations. We could then run the optimized RC models to reevaluate soil carbon storage for the transient 1% year^{-1} simulations. For this inverse approach, we optimized RC model parameters in each grid cell containing an observation site (Fig. 2, G and H, and figs. S8 and S9). We optimized the τ of the slowest pool and the corresponding transfer coefficient into this pool based on the ^{14}C observations while holding soil inputs and τ for the faster pools at their ESM-derived values. The size of the slowest carbon pool was constrained by optimizing the turnover time and the transfer coefficient together using both ^{14}C and total carbon. Consequently, the optimized RC model had about the same total carbon stock as the original ESM, thereby maintaining consistency with carbon inventory data.

EMBARGOED UNTIL 2PM U.S. EASTERN TIME ON THE THURSDAY BEFORE THIS DATE:

This optimization approach yielded τ_{slow} values of 3700 ± 2800 years for GFDL and 3500 ± 1300 years for HadGEM (using two-pool RC models), which were 16 to 17 times as long as the turnover times derived from the original ESMs.

For ESMs that included a passive pool, the optimization process yielded three distinct outcomes. For CESM, which has the largest passive pool (73% of soil carbon), the optimized $\tau_{passive}$ was 4500 years, which was 3.7 ± 1.5 times as long as $\tau_{passive}$ derived from the original model (Table 1). IPSL has a smaller fraction of passive carbon (46%) and therefore required a greater $\tau_{passive}$ (16,500 years) to obtain agreement with the observed $\Delta^{14}C$. For MRI, the passive pool size was too small (only 13% of soil carbon) to bring $\Delta^{14}C$ into alignment with the profile observations even after parameter optimization (fig. S10 and table S5). To adjust for MRI's potential bias in the passive pool size, we optimized r_f together with $\tau_{passive}$ and r_s to allow for simultaneous changes in slow and passive pool sizes. The resulting RC model for MRI was able to match observations (Fig. 2, G and H) with a passive pool fraction of 48% (see Methods and table S5). These results indicated that increasing the size and turnover time of the passive pool in ESMs would improve agreement with ^{14}C-based mean age estimates.

Bringing turnover time and carbon transfer parameters into agreement with ^{14}C observations had considerable consequences for the magnitude of the carbon-concentration feedback. Using the ^{14}C-based parameters, we conducted global transient simulations with each of the five RC models. These simulations showed that the soil as a whole (specifically the slow and passive pools) stored much less carbon in response to increasing levels of atmospheric CO_2, primarily as a consequence of reduced flow into the slow or passive pool. The soil carbon sink decreased from 32 ± 18% to 18 ± 12% (Table 1), corresponding to an absolute sink reduction of 170 ± 127 Pg C (Fig. 3). The magnitude of the soil sink reduction varied widely across the different models; those with larger and older passive fractions at the onset of the transient simulation (Table 1) generally had smaller sink reductions.

To assess the robustness of these sink reductions, we conducted a series of sensitivity experiments (see supplementary materials). We found that the sink reduction imposed by constraining the models with ^{14}C observations was robust to (i) turnover times optimized specifically for different biomes, (ii) spatial variation and magnitude of soil carbon stocks, and (iii) variations in $\Delta^{14}C$ across measurement sites (Table 2 and table S6). Sink reductions declined by a factor of 2 when the models were fit to an inventory that was 50% larger than the HWSD data set, suggesting that if soil carbon pools were larger in ESMs, ^{14}C-imposed sink reductions would be lower (*35*). Last, we used our RC model approach to analyze four fully coupled ESM runs (1pctCO_2) to address potential interactions between the carbon-climate and the carbon-concentration feedback. Constraints imposed by ^{14}C still reduced the sink by at least 40% on average (fig. S11 and table S7) in the fully coupled simulations (see supplementary materials).

We conclude that CMIP5 ESMs underestimated the mean age of soil carbon, especially for slow-cycling pools. By adjusting the turnover times of slow and passive pools to bring the models into alignment with ^{14}C observations, the potential for future soil carbon sequestration declined by 40 ± 27%. Although long-lived soil carbon pools consistent with old ^{14}C ages imply a similar potential for carbon storage at steady state, the time scale required to reach equilibrium is too long to mitigate the potentially damaging climate effects of rising CO_2 concentrations during the 21st century (fig. S2). These findings emphasize the need to incorporate ^{14}C and other diagnostics into ESM development and evaluation. In addition, models require better representation of long-term mechanisms of soil carbon stabilization such as organic matter-mineral interactions. Considered together with potential nutrient limitation of NPP inputs to soil (*36*), our analysis suggests that the carbon-concentration feedback may be weaker in the 21st century than currently expected from ESMs. Therefore, a greater fraction of CO_2 emissions than previously thought could remain in the atmosphere and contribute to global warming.

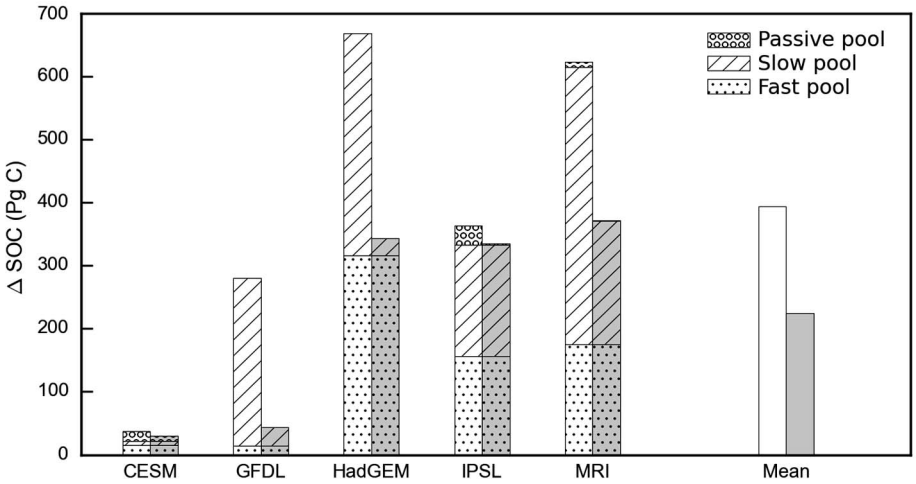

Fig. 3. Absolute change in SOC content from the reduced complexity model fit to the original ESM (bars with white background) and the estimate obtained by applying the ^{14}C constraint to the reduced complexity model (bars with gray background). The estimates on the right side show the total carbon content (sum of fast, slow, and passive) averaged across all the models, before and after applying the radiocarbon constraint.

REFERENCES AND NOTES

1. P. Friedlingstein *et al.*, *J. Clim.* **27**, 511–526 (2014).
2. IPCC, Summary for Policymakers. In *Climate Change 2013: The Physical Science Basis. Contribution of Working Group I to the Fifth Assessment Report of the Intergovernmental Panel on Climate Change*. T. F. Stocker *et al.*, Eds. (IPCC, Cambridge and New York, 2013).
3. V. K. Arora *et al.*, *J. Clim.* **26**, 5289–5314 (2013).
4. C. D. Jones, P. M. Cox, C. Huntingford, *Tellus B Chem. Phys. Meterol.* **58**, 603–613 (2006).
5. K. E. O. Todd-Brown *et al.*, *Biogeosciences* **11**, 2341–2356 (2014).
6. D. P. van Vuuren *et al.*, *Clim. Change* **109**, 5–31 (2011).
7. J. Lichter *et al.*, *Glob. Change Biol.* **14**, 2910–2922 (2008).
8. W. H. Schlesinger, J. Lichter, *Nature* **411**, 466–469 (2001).
9. J. W. Harden, R. K. Mark, E. T. Sundquist, R. F. Stallard, *Science* **258**, 1921–1924 (1992).
10. W. H. Schlesinger, *Nature* **348**, 232–234 (1990).
11. B. O'Brien, J. Stout, *Soil Biol. Biochem.* **10**, 309–317 (1978).
12. J. B. Gaudinski, S. E. Trumbore, E. A. Davidson, S. H. Zheng, *Biogeochemistry* **51**, 33–69 (2000).
13. M. S. Torn, S. E. Trumbore, O. A. Chadwick, P. M. Vitousek, D. M. Hendricks, *Nature* **389**, 170–173 (1997).
14. S. E. Trumbore, J. W. Harden, *J. Geophys. Res.* **102**, 28817–28830 (1997).
15. N. Carvalhais *et al.*, *Nature* **514**, 213–217 (2014).
16. A. D. Friend *et al.*, *Proc. Natl. Acad. Sci. U.S.A.* **111**, 3280–3285 (2014).
17. X. Wang *et al.*, *Glob. Change Biol.* **20**, 3229–3237 (2014).
18. W. Knorr, I. C. Prentice, J. I. House, E. A. Holland, *Nature* **433**, 298–301 (2005).
19. C. D. Koven *et al.*, *Biogeosciences* **12**, 5211–5228 (2015).
20. K. E. Taylor, R. J. Stouffer, G. A. Meehl, *Bull. Am. Meteorol. Soc.* **93**, 485–498 (2012).
21. J. A. Mathieu, C. Hatté, J. Balesdent, É. Parent, *Glob. Change Biol.* **21**, 4278–4292 (2015).
22. S. Trumbore, *Ecol. Appl.* **10**, 399–411 (2000).
23. W. Feng *et al.*, *Soil Biol. Biochem.* **100**, 118–124 (2016).
24. E. Shevliakova *et al.*, *Global Biogeochem. Cycles* **23**, GB2022 (2009).
25. M. W. Schmidt *et al.*, *Nature* **478**, 49–56 (2011).
26. M. Lützow *et al.*, *Eur. J. Soil Sci.* **57**, 426–445 (2006).
27. J. A. Dungait, D. W. Hopkins, A. S. Gregory, A. P. Whitmore, *Glob. Change Biol.* **18**, 1781–1796 (2012).
28. M. Kleber, R. Mikutta, M. S. Torn, R. Jahn, *Eur. J. Soil Sci.* **56**, 717–725 (2005).
29. J. S. Clemente, A. J. Simpson, M. J. Simpson, *Org. Geochem.* **42**, 1169–1180 (2011).
30. C. Koven *et al.*, *Biogeosciences* **10**, 7109–7131 (2013).
31. B. Ahrens, M. C. Braakhekke, G. Guggenberger, M. Schrumpf, M. Reichstein, *Soil Biol. Biochem.* **88**, 390–402 (2015).
32. G. B. Bonan, M. D. Hartman, W. J. Parton, W. R. Wieder, *Glob. Change Biol.* **19**, 957–974 (2013).
33. C. R. Lawrence, J. W. Harden, X. Xu, M. S. Schulz, S. E. Trumbore, *Geoderma* **247–248**, 73–87 (2015).
34. C. Rumpel, I. Kögel-Knabner, *Plant Soil* **338**, 143–158 (2011).

EMBARGOED UNTIL 2PM U.S. EASTERN TIME ON THE THURSDAY BEFORE THIS DATE:

35. Y. Luo *et al.*, *Global Biogeochem. Cycles* **30**, 40–56 (2016).
36. W. R. Wieder, C. C. Cleveland, W. K. Smith, K. Todd-Brown, *Nat. Geosci.* **8**, 441–444 (2015).

ACKNOWLEDGMENTS

We thank C. Hatté for sharing her compilation of published ^{14}C profiles. We received funding support from the Climate and Environmental Sciences Division of Biological and Environmental Research (BER) in the U.S. Department of Energy Office of Science. This included support from the Regional and Global Climate Modeling Program to the Biogeochemical Cycles Feedbacks Science Focus Area and several grants from the Terrestrial Ecosystem Science Program (DESC0014374 and DE-AC02-05CH11231). J.W.H. serves as chair of the science steering group for International Soil Carbon Network (http://iscn.fluxdata.org); however, the work of this publication reflects efforts on behalf of the U.S. Geological Survey Scientist Emeritus Program, which provided IT and infrastructure support. The model simulations analyzed in this study were obtained from the Earth System Grid Federation CMIP5 online portal hosted by the Program for Climate Model Diagnosis and Intercomparison at Lawrence Livermore National Laboratory (https://pcmdi.llnl.gov/projects/esgf-llnl/).

SUPPLEMENTARY MATERIALS

www.sciencemag.org/content/353/6306/1419/suppl/DC1
Materials and Methods
Sensitivity Analysis Results
Fully Coupled Simulation Analysis
Figs. S1 to S11
Tables S1 to S7
References (*37–102*)

27 September 2015; accepted 29 August 2016
10.1126/science.aad4273

ATMOSPHERIC SCIENCE

An unexpected disruption of the atmospheric quasi-biennial oscillation

Scott M. Osprey,[1]* Neal Butchart,[2] Jeff R. Knight,[2] Adam A. Scaife,[2,3] Kevin Hamilton,[4] James A. Anstey,[5] Verena Schenzinger,[1] Chunxi Zhang[4]

One of the most repeatable phenomena seen in the atmosphere, the quasi-biennial oscillation (QBO) between prevailing eastward and westward wind jets in the equatorial stratosphere (approximately 16 to 50 kilometers altitude), was unexpectedly disrupted in February 2016. An unprecedented westward jet formed within the eastward phase in the lower stratosphere and cannot be accounted for by the standard QBO paradigm based on vertical momentum transport. Instead, the primary cause was waves transporting momentum from the Northern Hemisphere. Seasonal forecasts did not predict the disruption, but analogous QBO disruptions are seen very occasionally in some climate simulations. A return to more typical QBO behavior within the next year is forecast, although the possibility of more frequent occurrences of similar disruptions is projected for a warming climate.

Aside from those variations governed by the changing seasons or diurnal cycle, the quasi-biennial oscillation (QBO) is arguably the most repeatable mode of natural variability seen anywhere in the atmosphere. It was first discovered in the late 1950s (*1*, *2*) and features alternating eastward and westward wind jets descending through the equatorial stratosphere at roughly 1 km per month (*3*), from ~50 km (~1 hPa) down to ~16 km (~100 hPa), with the quasi-biennial periodicity being most evident in the ~20- to 40-km layer. Since the 1950s, the period of the oscillation has varied between 22 to 36 months. The oscillation is nearly zonally uniform and so is seen in both local observations and in longitudinally averaged data with roughly the same amplitude, at least for monthly means, and is confined to equatorial latitudes (*4*, *5*). On the other hand, its influence is felt throughout the atmosphere. For example, the fate of ash and sulfur from large volcanic eruptions in the tropics is affected by the QBO (*6*), and there are known surface weather and climate impacts resulting from the QBO's extratropical teleconnections (*7*–*9*); such teleconnections may provide an important source of predictability that can be exploited with seasonal and decadal prediction systems (*10*) owing to the regularity of the QBO. Disruption to the regular QBO behavior is therefore expected to have potentially far-reaching consequences.

In November 2015, the QBO winds were westward above 30 km (~15 hPa) and eastward beneath. During November and December 2015, the westward phase propagated downward as is typical (Fig. 1A), but by January 2016, its descent had stalled. Although by itself this was not unusual (Fig. 1A, during early 2009, just above 20 hPa), the stalling was followed by the unexpected formation of a second westward layer interrupting the lower stratospheric eastward phase (near 40 hPa). Subsequently, the descending westward phase in the upper stratosphere began to recede, while the anomalous westward jet below strengthened and began to descend. Here, we quantify the extent to which this behavior is anomalous compared with the previous six decades of observations containing 27 QBO cycles.

The state of the QBO is often characterized by using an updated time series of monthly mean balloon observations of near-equatorial zonal winds (*11*). This record spans essentially the entire era of operational tropical stratospheric wind soundings from January 1956 to present day and provides 724 monthly profiles of the equatorial zonal wind. For each of these profiles, we identified a "best match" month having the smallest root mean square (RMS) difference over seven levels spanning 70 to 10 hPa (Fig. 1B). For the vast majority of months, there is a close match with another month in the record, and RMS differences are typically 2 to 3 ms^{-1}. Before 2016, the month with the largest RMS difference with its best historical match was December 1988 (4.8 ms^{-1}). The unprecedented behavior in 2016 is apparent because February, March, and April 2016 have RMS differences of 6.7, 10.1, and 6.8 ms^{-1}, respectively.

Canonical theory describes the QBO as driven by the interaction of the zonal mean flow, with a spectrum of vertically propagating waves forced in the lower atmosphere and dissipated within the stratosphere (*12*, *13*). Mean-flow driving is proportional to local vertical wind shear so that where there is westward vertical shear, the mean flow is accelerated westward, and vice versa for eastward vertical shear. This leads to the downward phase propagation of the alternating QBO wind regimes seen throughout the observed record (Fig. 1A). The selective filtering of upward propagating waves by low-level jets then leads to opposite-sign acceleration at higher levels in a "shadowing effect." Climatological large-scale upwelling in the equatorial stratosphere (*14*) opposes the downward phase propagation (*15*) and can contribute to the descent stalling, whereas the forcing of the westward phase can be supplemented by horizontally propagating quasi-stationary planetary waves from the extratropics, particularly in boreal winter (*16*–*19*).

Because the strong westward accelerations near 30 to 50 hPa in late 2015 and early 2016 occur in a region of eastward mean flow shear, they cannot be accounted for by the canonical theory. On the other hand, fluxes of wave activity (Fig. 2A, arrows) averaged for February 2016 suggest that waves propagating from the Northern Hemisphere might be the most likely cause of the westward acceleration (planetary scale Rossby waves propagating from the extratropics can only transport westward momentum). Typically, during winter months upward wave activity fluxes enter the stratosphere at mid- to high latitudes then refract equatorward. In February 2016, the anomalously strong high-latitude eastward jet was unusually flanked by subtropical

[1]National Centre for Atmospheric Science (NCAS)–Climate, University of Oxford, Atmospheric, Oceanic and Planetary Physics, Clarendon Laboratory, Parks Road, Oxford, OX1 3PU, UK. [2]Met Office Hadley Centre, FitzRoy Road, Exeter, Devon, EX1 3PB, UK. [3]Department of Mathematics and Computer Science, University of Exeter, Exeter, UK. [4]International Pacific Research Center, University of Hawai`i, Honolulu, USA. [5]Canadian Centre for Climate Modelling and Analysis, University of Victoria, Victoria, British Columbia, Canada.
*Corresponding author. Email: scott.osprey@physics.ox.ac.uk

EMBARGOED UNTIL 2PM U.S. EASTERN TIME ON THE THURSDAY BEFORE THIS DATE: